



# Observations of Forbush Decreases of Cosmic-Ray Electrons and Positrons with the Dark Matter Particle Explorer

Francesca Alemanno<sup>1,2</sup>, Qi An<sup>3,4</sup>, Philipp Azzarello<sup>5</sup>, Felicia Carla Tiziana Barbato<sup>1,2</sup>, Paolo Bernardini<sup>6,7</sup>, XiaoJun Bi<sup>8,9</sup>, MingSheng Cai<sup>10,11</sup>, Elisabetta Casilli<sup>6,7</sup>, Enrico Catanzani<sup>12</sup>, Jin Chang<sup>10,11</sup>, DengYi Chen<sup>10</sup>, JunLing Chen<sup>13</sup>, ZhanFang Chen<sup>10,11</sup>, MingYang Cui<sup>10</sup>, TianShu Cui<sup>14</sup>, YuXing Cui<sup>10,11</sup>, HaoTing Dai<sup>3,4</sup>, Antonio De Benedittis<sup>6,7</sup>, Ivan De Mitri<sup>1,2</sup>, Francesco de Palma<sup>6,7</sup>, Maksym Deliyergiyev<sup>5</sup>, Margherita Di Santo<sup>1,2</sup>, Qi Ding<sup>10,11</sup>, TieKuang Dong<sup>10</sup>, ZhenXing Dong<sup>14</sup>, Giacinto Donvito<sup>15</sup>, David Droz<sup>9</sup>, JingLai Duan<sup>13</sup>, KaiKai Duan<sup>10</sup>, Domenico D'Urso<sup>12,20</sup>, RuiRui Fan<sup>9</sup>, YiZhong Fan<sup>10,11</sup>, Fang Fang<sup>13</sup>, Kun Fang<sup>9</sup>, ChangQing Feng<sup>3,4</sup>, Lei Feng<sup>10</sup>, Piergiorgio Fusco<sup>15,16</sup>, Min Gao<sup>9</sup>, Fabio Gargano<sup>15</sup>, Ke Gong<sup>9</sup>, YiZhong Gong<sup>10</sup>, DongYa Guo<sup>9</sup>, JianHua Guo<sup>10,11</sup>, ShuangXue Han<sup>14</sup>, YiMing Hu<sup>10</sup>, GuangShun Huang<sup>3,4</sup>, XiaoYuan Huang<sup>10,11</sup>, YongYi Huang<sup>10</sup>, Maria Ionica<sup>12</sup>, Wei Jiang<sup>10</sup>, Jie Kong<sup>13</sup>, Andrii Kotenko<sup>5</sup>, Dimitrios Kyratzis<sup>1,2</sup>, S. Li<sup>10,21</sup>, ShiJun Lei<sup>10</sup>, WenHao Li<sup>10,11</sup>, WeiLiang Li<sup>14</sup>, Xiang Li<sup>10,11</sup>, XianQiang Li<sup>14</sup>, YaoMing Liang<sup>14</sup>, ChengMing Liu<sup>3,4</sup>, Hao Liu<sup>10</sup>, Jie Liu<sup>13</sup>, ShuBin Liu<sup>3,4</sup>, Yang Liu<sup>10</sup>, Francesco Loparco<sup>15,16</sup>, ChuanNing Luo<sup>10,11</sup>, Miao Ma<sup>14</sup>, PengXiong Ma<sup>10</sup>, Tao Ma<sup>10</sup>, XiaoYong Ma<sup>14</sup>, Giovanni Marsella<sup>6,7,22</sup>, Mario Nicola Mazziotta<sup>15</sup>, Dan Mo<sup>13</sup>, XiaoYang Niu<sup>13</sup>, Xu Pan<sup>10,11</sup>, Andrea Parenti<sup>1,2</sup>, WenXi Peng<sup>9</sup>, XiaoYan Peng<sup>10</sup>, Chiara Perrina<sup>5,23</sup>, Rui Qiao<sup>9</sup>, JiaNing Rao<sup>14</sup>, Arshia Ruina<sup>5</sup>, MariaMunoz Salinas<sup>5</sup>, Zhi Shangguan<sup>14</sup>, WeiHua Shen<sup>14</sup>, ZhaoQiang Shen<sup>10</sup>, ZhongTao Shen<sup>3,4</sup>, Leandro Silveri<sup>1,2</sup>, JingXing Song<sup>14</sup>, Mikhail Stolpovskiy<sup>5</sup>, Hong Su<sup>13</sup>, Meng Su<sup>17</sup>, HaoRan Sun<sup>3,4</sup>, ZhiYu Sun<sup>13</sup>, Antonio Surdo<sup>7</sup>, XueJian Teng<sup>14</sup>, Andrii Tykhonov<sup>5</sup>, JinZhou Wang<sup>9</sup>, LianGuo Wang<sup>14</sup>, Shen Wang<sup>10</sup>, ShuXin Wang<sup>10,11</sup>, XiaoLian Wang<sup>3,4</sup>, Ying Wang<sup>3,4</sup>, YanFang Wang<sup>3,4</sup>, YuanZhu Wang<sup>10</sup>, DaMing Wei<sup>10,11</sup>, JiaJu Wei<sup>10</sup>, YiFeng Wei<sup>3,4</sup>, Di Wu<sup>9</sup>, Jian Wu<sup>10,11</sup>, LiBo Wu<sup>1,2</sup>, Sha Sha Wu<sup>14</sup>, Xin Wu<sup>5</sup>, ZiQing Xia<sup>10</sup>, EnHeng Xu<sup>3,4</sup>, HaiTao Xu<sup>14</sup>, ZhiHui Xu<sup>10,11</sup>, ZunLei Xu<sup>10</sup>, GuoFeng Xue<sup>14</sup>, ZiZong Xu<sup>3,4</sup>, HaiBo Yang<sup>13</sup>, Peng Yang<sup>13</sup>, YaQing Yang<sup>13</sup>, Hui Jun Yao<sup>13</sup>, YuHong Yu<sup>13</sup>, GuanWen Yuan<sup>10,11</sup>, Qiang Yuan<sup>10,11</sup>, Chuan Yue<sup>10</sup>, JingJing Zang<sup>10,18</sup>, ShengXia Zhang<sup>13</sup>, WenZhang Zhang<sup>14</sup>, Yan Zhang<sup>10</sup>, Yi Zhang<sup>10,11</sup>, YongJie Zhang<sup>13</sup>, YunLong Zhang<sup>3,4</sup>, YaPeng Zhang<sup>13</sup>, YongQiang Zhang<sup>10</sup>, ZhiYong Zhang<sup>3,4</sup>, Zhe Zhang<sup>10</sup>, Cong Zhao<sup>3,4</sup>, HongYun Zhao<sup>13</sup>, XunFeng Zhao<sup>14</sup>, ChangYi Zhou<sup>14</sup>, Yan Zhu<sup>14</sup>

(DAMPE Collaboration),


Wei Chen<sup>10</sup>, Li Feng<sup>10</sup>, Xi Luo<sup>19</sup>, and ChengRui Zhu<sup>10</sup><sup>1</sup> Gran Sasso Science Institute (GSSI), Via Iacobucci 2, I-67100 L'Aquila, Italy<sup>2</sup> Istituto Nazionale di Fisica Nucleare (INFN) - Laboratori Nazionali del Gran Sasso, I-67100 Assergi, L'Aquila, Italy<sup>3</sup> State Key Laboratory of Particle Detection and Electronics, University of Science and Technology of China, Hefei 230026, People's Republic of China<sup>4</sup> Department of Modern Physics, University of Science and Technology of China, Hefei 230026, People's Republic of China<sup>5</sup> Department of Nuclear and Particle Physics, University of Geneva, CH-1211, Switzerland<sup>6</sup> Dipartimento di Matematica e Fisica E. De Giorgi, Università del Salento, I-73100, Lecce, Italy<sup>7</sup> Istituto Nazionale di Fisica Nucleare (INFN) - Sezione di Lecce, I-73100, Lecce, Italy<sup>8</sup> University of Chinese Academy of Sciences, Yuquan Road 19A, Beijing 100049, People's Republic of China<sup>9</sup> Particle Astrophysics Division, Institute of High Energy Physics, Chinese Academy of Sciences, Beijing 100049, People's Republic of China<sup>10</sup> Key Laboratory of Dark Matter and Space Astronomy, Purple Mountain Observatory, Chinese Academy of Sciences, Nanjing 210023, People's Republic of China<sup>11</sup> School of Astronomy and Space Science, University of Science and Technology of China, Hefei 230026, People's Republic of China<sup>12</sup> Istituto Nazionale di Fisica Nucleare (INFN) - Sezione di Perugia, I-06123 Perugia, Italy<sup>13</sup> Institute of Modern Physics, Chinese Academy of Sciences, Lanzhou 730000, People's Republic of China<sup>14</sup> National Space Science Center, Chinese Academy of Sciences, Nanertiao 1, Zhongguancun, Haidian district, Beijing 100190, People's Republic of China<sup>15</sup> Istituto Nazionale di Fisica Nucleare, Sezione di Bari, via Orabona 4, I-70126 Bari, Italy<sup>16</sup> Dipartimento di Fisica M. Merlin, dell'Università e del Politecnico di Bari, via Amendola 173, I-70126 Bari, Italy<sup>17</sup> Department of Physics and Laboratory for Space Research, the University of Hong Kong, Pok Fu Lam, Hong Kong SAR, People's Republic of China<sup>18</sup> School of Physics and Electronic Engineering, Linyi University, Linyi 276000, People's Republic of China; [zangjingjing@lyu.edu.cn](mailto:zangjingjing@lyu.edu.cn)<sup>19</sup> Shandong Institute of Advanced Technology, 250100 Jinan, People's Republic of China

Received 2021 August 26; revised 2021 September 30; accepted 2021 October 5; published 2021 October 22

## Abstract

The Forbush decrease (FD) represents the rapid decrease of the intensities of charged particles accompanied with the coronal mass ejections or high-speed streams from coronal holes. It has been mainly explored with the ground-based neutron monitor network, which indirectly measures the integrated intensities of all species of cosmic rays by counting secondary neutrons produced from interaction between atmospheric atoms and cosmic rays. The

space-based experiments can resolve the species of particles but the energy ranges are limited by the relatively small

 Original content from this work may be used under the terms of the [Creative Commons Attribution 4.0 licence](https://creativecommons.org/licenses/by/4.0/). Any further distribution of this work must maintain attribution to the author(s) and the title of the work, journal citation and DOI.

<sup>23</sup> Also at: Institute of Physics, Ecole Polytechnique Federale de Lausanne (EPFL), CH-1015 Lausanne, Switzerland.

acceptances except for the most abundant particles like protons and helium. Therefore, the FD of cosmic-ray electrons and positrons have just been investigated by the PAMELA experiment in the low-energy range ( $<5$  GeV) with limited statistics. In this paper, we study the FD event that occurred in 2017 September with the electron and positron data recorded by the Dark Matter Particle Explorer. The evolution of the FDs from 2 GeV to 20 GeV with a time resolution of 6 hr are given. We observe two solar energetic particle events in the time profile of the intensity of cosmic rays, the earlier, and weaker, one has not been shown in the neutron monitor data. Furthermore, both the amplitude and recovery time of fluxes of electrons and positrons show clear energy dependence, which is important in probing the disturbances of the interplanetary environment by the coronal mass ejections.

*Unified Astronomy Thesaurus concepts:* [Solar coronal mass ejections \(310\)](#); [Forbush effect \(546\)](#); [Cosmic rays \(329\)](#)

## 1. Introduction

Charged solar wind particles and the associated magnetic fields affect the transportation of Galactic cosmic rays (GCRs) in the solar system. Violent solar activities like coronal mass ejections (CMEs) generate high-intensity particle flows moving at super-Alfvén speed, which enhance the local interplanetary magnetic field significantly. Such temporarily enhanced magnetic fields would block the propagation of GCRs, which contributes to sharp decreases of the GCR fluxes, known as Forbush decreases (FDs; Forbush 1937; Hess & Demmel-mair 1937). The FD is a universal phenomenon within the heliosphere, which was also observed at other planets, e.g., Mars (Guo et al. 2018), and the interplanetary space far away from the Sun (e.g., by Voyager 2 Burlaga 2015).

Precise measurements of FDs will enable us to diagnose the propagation of GCRs and their interplay with the complex environment in the heliosphere. FDs of GCRs have been extensively measured for decades with worldwide ground-based neutron monitors (NMs) located at regions with different geomagnetic cutoff rigidities. Compared with direct detection experiments, the NMs can only reflect an integral variation of the incident particle intensities, with much information regarding the compositions and precise energy-dependencies being lost. In the 1960s, some balloon experiments (Meyer & Vogt 1961) measured FDs of electrons and protons at MeV energies. However, the relatively poor energy resolution, bad particle identification, and limited statistics hindered a good understanding of FDs of various particle species. Recently, the PAMELA experiment simultaneously measured FDs of protons, helium nuclei, and electrons for the first time, and found important differences in the properties of different particle species (Munini et al. 2018). Specifically, the recovery time for electrons is faster than that for protons and helium nuclei, which may be interpreted as a charge-sign-dependent drift pattern between electrons and nuclei (Munini et al. 2018). However, due to its relatively small geometry factor, the data statistics is limited (particularly for electrons), and the energy dependence of the FD characteristics remains somehow ambiguous.

The Dark Matter Particle Explorer (DAMPE) is a space-borne detector for observations of cosmic-ray electrons and positrons (CREs), nuclei, and  $\gamma$ -ray photons (Chang et al. 2017; DAMPE Collaboration et al. 2017; An et al. 2019). The DAMPE is optimized for high-energy-resolution measurements of CREs. Compared with other particle detectors in orbit, the DAMPE has two unique advantages in the measurements of time variations of CRE fluxes: (1) the inclination angle of the orbit is  $97^\circ$  (Chang et al. 2017), and thus DAMPE can reach the Earth's polar regions where GCRs are weakly affected by the geomagnetic rigidity cutoff, and (2) the relatively large

effective geometry acceptance ( $\sim 0.35$  m<sup>2</sup>sr) enables a more detailed study of the fine time structures of FDs. Benefiting from these two facts, in this work we present the observations of FDs of CREs by DAMPE with unprecedented accuracy and give solid evidence of energy dependences for both the FD amplitude and the recovery time.

This paper mainly focuses on a strong FD event that occurred in 2017 September when two shock-associated interplanetary coronal mass ejections (ICMEs) and a ground level enhancement (GLE) were also detected by ground-based NMs. The solar flares in 2017 September are very famous events. Based on the NM data, Badruddin et al. (2019) presented a 3–4 hr time-lagged correlation between cosmic-ray intensities and the geomagnetic activity indices. Hubert et al. (2019) presented cosmic-ray-induced neutron spectra during an active solar event leading to changes in the local cosmic-ray spectrum (FDs and a GLE). Meanwhile, by calculating the GCR spectral index of FDs, several theoretical yield functions were verified in Livada & Mavromichalaki (2020) and referenced therein. Chertok et al. (2018) analyzed space weather disturbance and successfully estimated the scale of FD and geomagnetic storm.

## 2. DAMPE Detector

The DAMPE satellite operates in a Sun-synchronous orbit at 500 km altitude with a period of 5673 s and an inclination angle of  $97^\circ$  that enables the satellite to travel the area from  $83^\circ$  north to  $83^\circ$  south. The detector system consists of four subdetectors (Chang et al. 2017). At the top is a plastic scintillator array detector (PSD) that measures the ionization energy loss of charged particles and also acts as an anticoincidence veto detector for identification of photon candidates (Yu et al. 2017). The instrument mounted below PSD is a silicon tungsten tracker (STK) equipped with 12 layers of  $121 \mu\text{m}$  wide silicon strip sensors (Azzarello et al. 2016). STK is designed to measure the trajectory and charge of a charged particle and to convert  $\gamma$ -rays into  $e^+e^-$  pairs. The core detector of DAMPE is a Bismuth Germanate (BGO) calorimeter, which has a thickness of BGO crystals of 32 radiation length, that measures the energy and direction of a particle to distinguish hadronic and electromagnetic particle species and also to provide the trigger for the data acquisition (DAQ) system (Zhang et al. 2015). The dense and thick materials of the BGO provide an excellent energy resolution for CREs, which is about 5% (2%) at  $\sim 2$  (20) GeV (Zhang et al. 2016). At the bottom is a neutron detector (NUD), which is used to improve the capability of hadron-nuclei separation, since many more neutrons are generated in the hadronic shower. The on-orbit performance of each subdetector can be found elsewhere

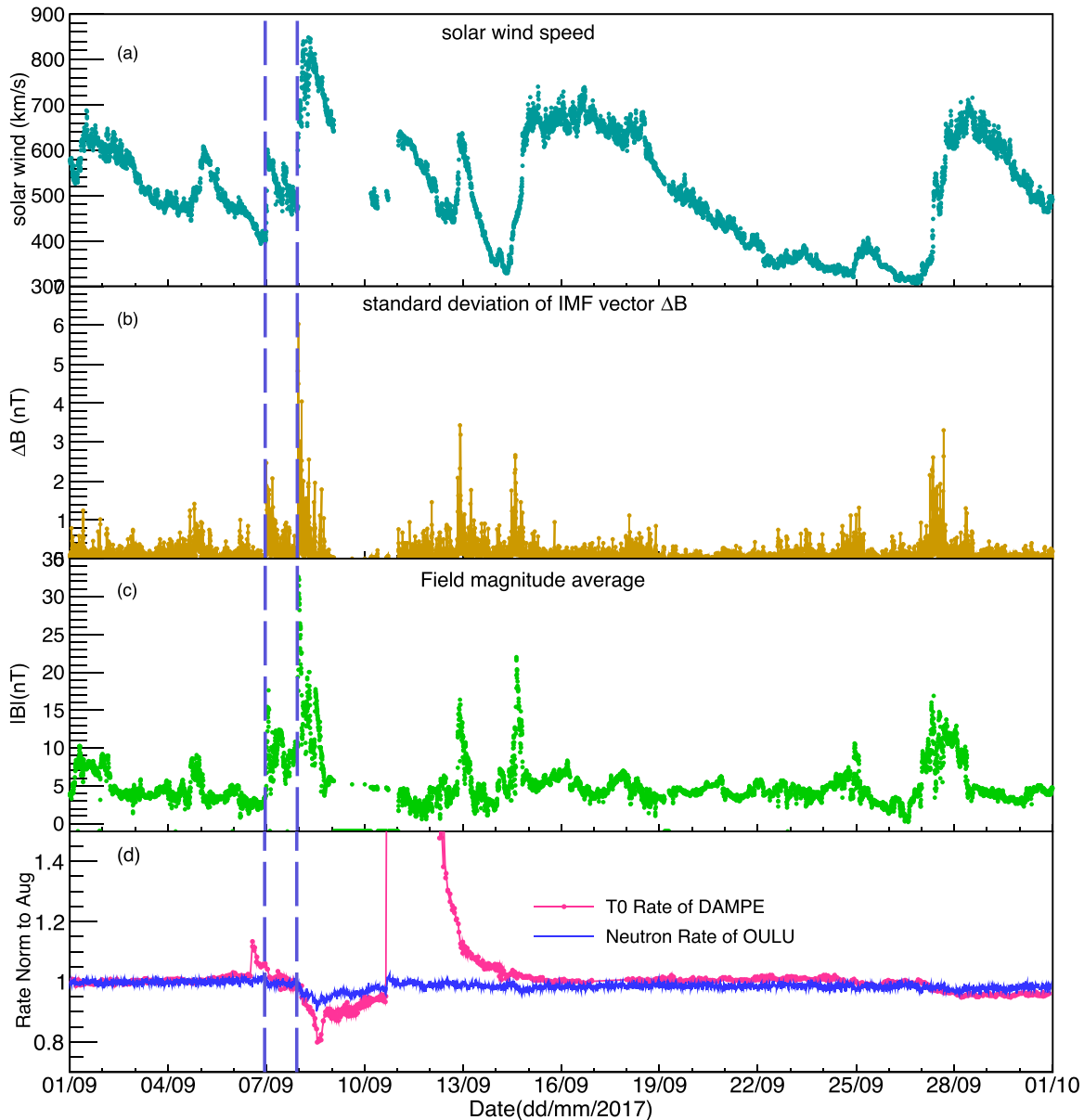


**Figure 1.** The 5 minute average time profiles of the solar wind speed (panel (a)), the standard deviation of the IMF vector (panel (b)), and the average strength of the IMF at 1 au (panel (c)). Data in panels (a), (b), and (c) are all from the OMNI database ([https://omniweb.gsfc.nasa.gov/form/omni\\_min.html](https://omniweb.gsfc.nasa.gov/form/omni_min.html)). Panel (d) shows the 47 minute average temporal variation of the T0 counting rate of DAMPE for  $4.76 < L < 5.57$  (rate is normalized to the average value in 2017 August). Also shown in panel (d) is the OULU NM 10 minute average relative counting rate with respect to the average value in 2017 August (data from <http://www01.nmdb.eu/nest/>). The two vertical red lines indicate the arrival times of the interplanetary shocks.

(Tykhonov et al. 2018; Ambrosi et al. 2019; Ma et al. 2019; Tykhonov et al. 2019; Huang et al. 2020).

### 3. Data Analysis

We describe the time variation of the GCRs due to the CME event at two levels, the counting rate from the T0 counts (a category of data acquisition trigger with very loose threshold, see below for details) and the absolute fluxes of CREs. The T0 counting rate measures the overall intensity of all species of GCRs above 100 MeV with an average of 48 minute (half orbit period) time resolution, which enabled DAMPE to discover fine structures of time profile of GCR intensity. Meanwhile, the absolute flux variations of CREs in dozens of energy intervals are simultaneously measured for the purpose of investigating the energy dependence of the FD characteristics.

#### 3.1. T0 Counting Rate

During the on-orbit operation of DAMPE, the housekeeping system records GCR trigger counts every 4 s (the so-called T0 trigger count) for the purpose of monitoring the health of detectors. T0 is a low threshold hit signal acting as the timing reference to decide when to start recording event data. Based on the Geant4 simulation, GCRs with kinematic energy above 100 MeV can satisfy the T0 trigger logic. Because T0 does not record information of particle species, its counting rate reflects the overall intensity of all kinds of GCRs above 100 MeV. On DAMPE's orbit, the T0 counting rate changes from several hundred Hz near the equator to several thousand Hz at the poles. We would like to compare the DAMPE T0 counting rate with the NM data. Since the NMs are fixed on the surface of the Earth, and DAMPE keeps moving along its orbit, we select the

T0 counting rate in a narrow region with the specific McIlwain  $L$ -parameter values (Walt 2005) where geomagnetic cutoff rigidity is assumed to be a constant. For the OULU NM that we adopt in the comparison, we find that for  $4.76 < L < 5.57$  the averaged cutoff rigidity is  $R_c \approx 0.81$  GV, which is similar to that of the OULU station. Panel (d) of Figure 1 shows the time evolutions (normalized to the average values in 2017 August) of the DAMPE T0 rate (red) and the OULU NM rate (blue) in 2017 September. A 27 day long-term shallow change of the T0 rate has been subtracted by dividing the rate by a smooth polynomial fitting form to the T0 counts from August 23 to September 24 after abandoning the FD time range. Also shown in Figure 1 are 5 minute averaged time profiles of the solar wind speed (panel (a)), the standard deviation of the interplanetary magnetic field (IMF) vector (panel (b)), and the average strength of the IMF (panel (c)). Two vertical lines label the arrival times<sup>24</sup> of two interplanetary shocks, at 23:02 UT, 2017 September 6, and 22:28 UT, 2018 September 7.

From the T0 counting rate, we can clearly identify two solar energetic particle (SEP) events. The first one with smaller amplitude reached the Earth 10–11 hr before the interplanetary shock wave and lasted for about 20 hr. However, the NM data (from OULU and others) did not show such a rise for this event (see panel (d) of Figure 1). The reason for the difference between NMs and the direct measurements is unclear. One reason might be that DAMPE is not blocked by the atmosphere and is more sensitive to low-energy particles than NM stations. The other possible explanation is the anisotropy of SEPs, which may lead to NMs missing the detection. We also investigate the time profiles of the T0 counts at high latitudes (with  $L > 4.11$ ) in both southern and northern hemispheres, and such intensity enhancements are both observed. About 89 hr after the arrival of the second shock (during the recovery phase of the FD), the T0 counting rate further shows a sudden and big jump (increased by 2 orders of magnitude), which indicates the arrival of the second SEP event. At that moment the OULU NM also observed a GLE event with a several percent increase in the counting rate. The big difference of the SEP amplitudes between DAMPE and OULU is again a reflection that NMs are only sensitive to high enough energy particles.

When SEPs pass by the Earth (UT 0906-23:02 to 0910-16:03) the fluxes of energetic particles are so high that the detector cannot operate in the normal status any more due to significant and random shifts in the pedestals of the electronics. Thus the scientific data taken in this period has been excluded in the current analysis.

### 3.2. CRE Fluxes

For the purpose of this study, about 60 days of DAMPE data, in total 300 million events, recorded in 2017 August and September are analyzed. To make sure the detector operates in good condition, the data recorded when DAMPE passes through the South Atlantic Anomaly (SAA) region are excluded.

We apply a series of selection criteria to filter a clean sample of CREs. The purpose of this is to suppress the background cosmic rays as much as possible while keeping a sufficiently high CRE efficiency. The first step of the preselections is to require that the BGO bar with the maximum deposited energy in each layer is not at the edge of the BGO calorimeter, which

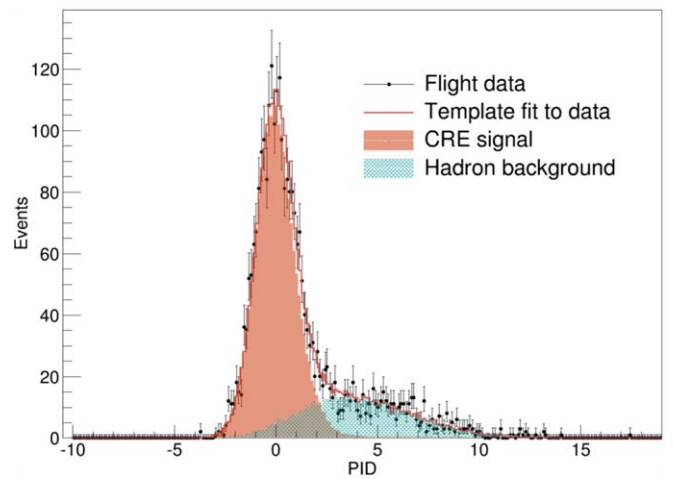


**Figure 2.** Distributions of the PID variable for the deposited energy bin  $4.83 \text{ GeV} < E < 5.25 \text{ GeV}$ . The best-fit MC templates are also shown for comparison. Setting the PID selection value of  $< 2$  results in a background contamination of  $\sim 8\%$ .

can make sure that most of the shower energies are recorded by the calorimeter and a good energy resolution is guaranteed. Then a track selection and evaluation strategy very similar to that described in Xu et al. (2018) is adopted to identify the tracks of events. Specifically, the STK track should be a long track crossing all layers of STK and match the BGO track, and the CRE should deposit most energy within a 5 mm cylinder around the track. Once the track is determined, the charge of the particle can be obtained via the charge reconstruction algorithm (Dong et al. 2019). Here we require the charge number measured by PSD to be less than 1.7, which can reject  $Z \geq 2$  nuclei up to a level of 99%. Finally, to eliminate secondary particles generated in the atmosphere, the minimum energy at each geomagnetic latitude is required to exceed 1.2 times the vertical rigidity cutoff (VRC; Smart & Shea 2005).

The preselections can already strongly exclude heavy nuclei from the sample. However, there is still heavy contamination from protons and also helium nuclei. Based on the shower development in the calorimeter, a particle identification (PID) variable is constructed.

$$\text{PID} = F(E)[\log(\text{RMS}_r)\sin\theta + \log(\text{RMS}_l)\cos\theta],$$

where  $F(E)$  is the energy decoupling polynomial,  $\theta$  is the coordinate rotation angle, and  $\text{RMS}_r$  and  $\text{RMS}_l$  are functions describing radial shower shape and longitudinal shower shape, respectively.

The background contamination can then be estimated through a fitting with Monte Carlo (MC) templates in each energy bin, as illustrated in Figure 2. The background contamination is estimated to be  $2\% \sim 8\%$  for events with deposited energies between 2 GeV and 20 GeV. Below 2 GeV, the granularity of the calorimeter does not allow us to efficiently identify CREs from nuclei. Since the low-energy particles are modulated by solar winds, their fluxes show slight and continuous variations with time. We thus estimate the background in each time bin. It is found that the hadronic background varies by  $\sim 6\%$  at 2 GeV and  $\sim 1\%$  at 20 GeV. After the preselections and the PID procedure, the CRE candidate events are divided into 25 logarithmically even energy bins from 2 GeV to 20 GeV and 240 time bins (6 hr

<sup>24</sup> Data from the Cfa Interplanetary Shock Database: [www.caf.harvard.edu](http://www.caf.harvard.edu).

each). The statistical errors in two-dimensional bins are about 2% at 5 GeV and  $\sim 8\%$  at 20 GeV.

Due to the shielding effect of the geomagnetic field, primary GCRs can only be detected when their rigidities are larger than the cutoff rigidity. A threshold of  $1.2 \times \text{VRC}$  is adopted to minimize such an effect. Since the VRC varies with locations of the detector, the effective exposure time thus changes with particle rigidity/energy. In each energy bin and time bin, the exposure time is calculated via summarizing the time when the satellite travels in the regions with VRC values smaller than  $1/1.2$  of the lower edge of the energy bin, with an additional subtraction of the dead time of the DAQ system and the time when DAMPE passes through the SAA region or under the calibration operations. On average the effective exposure time is about 80% of the total time for energies above 15 GeV, which gradually decreases to  $\sim 30\%$  at 2 GeV.

The CRE flux in the  $i$ th energy bin and  $j$ th time bin can be calculated as

$$\Phi_{i,j} = \frac{N_{i,j}(1 - f_{i,j})}{A_i \eta_{i,j} \Delta T_j \Delta E_i}, \quad (1)$$

where  $N_{i,j}$ ,  $f_{i,j}$ , and  $\eta_{i,j}$  represent the number of CRE candidates, the fraction of the background contamination, and the trigger efficiency,  $A_i$  is the effective acceptance of the detector,  $\Delta T_j$  is the live time, and  $\Delta E_i$  is the width of the energy bin. In this analysis we focus on the relative fluxes of CREs in a timescale of 3 months, and therefore the absolute efficiencies are not crucial.

The dominating systematic uncertainty of the relative flux ratio measurements comes from the stability of efficiencies. An extensive study of the efficiency variations have been performed in this analysis. As shown in Ambrosi et al. (2019), the major calibration parameters, including the pedestals, dynode ratios, electronics gains, MIP energies, etc., are very stable after the temperature correction (with variations of  $< 1.5\%$  per year). Therefore the detection efficiency change within 1 month is expected to be very small (0.13%). On the other hand, due to the radiation damage and aging electronics, the light yields of the BGO crystals and the gains of photomultipliers are found to slightly decrease over time. Their impacts on the trigger threshold of each BGO crystal are carefully calibrated, which shows a decrease of  $\sim 1.25\%$  per year. We further investigate the impact of the trigger efficiency from the potential bias of the energy scale through applying a series of bias factors from  $-5\%$  to  $+5\%$  with a step of 1% in the MC simulation, and find that the change of trigger efficiency within 1 month is also small (0.5% at 2 GeV; 0.01% at 20 GeV). The other efficiency is the track efficiency of the STK. Since we employ track selection at different moments of 2017, we estimate the corresponding stability of the tracking, using proton flight data samples. Our results confirm the high stability of the tracking efficiency, with the overall variations throughout the data taking period being less than 0.2% per year.

In summary, the total systematic uncertainty of the relative detection and selection efficiencies is about 0.53%, which is much smaller than the statistical errors (2%  $\sim$  8%).

#### 4. Time Profiles of CRE Fluxes

We calculate the CRE fluxes with a time bin width of 6 hr (about four orbits for DAMPE). The flux of each bin is

normalized to the average flux of 2017 August. The time profiles of four selected energy bins are shown in Figure 3. As we have discussed in Section 3.1, the data from 18:00 UT of September 9 to 12:00 UT of September 11 have been eliminated due to the strong impact from the energetic particles from the SEP. The relative intensities averaged over 10 minutes from the OULU NM<sup>25</sup> are also plotted in Figure 3.

Compared with the T0 rates, we do not find a significant increase in the CRE fluxes during the first SEP event. One possible reason is that the data statistics is limited, and the population of SEP above GeVs is not significant. The NM data do not show the SEP event either. The physical interpretation of such differences may need further study.

Similar to the PAMELA experiment (Munini et al. 2018) we use the following function

$$\frac{\Phi(t)}{\Phi_{\text{ref}}} = 1 - A_e \exp\left(-\frac{t - t_0}{\tau}\right), \quad (2)$$

to describe the amplitude and recovery behavior after the CRE fluxes reach the valley. In the above equation,  $\Phi_{\text{ref}}$  is the reference flux of 2017 August, and  $A_e$ ,  $\tau$ , and  $t_0$  represent the decrease amplitude, recovery time, and time of the minimum flux (or the start of the recovery phase), respectively. For this event,  $t_0$  is fixed to be 13:30 UT of 2017 September 8.  $A_e$  and  $\tau$  parameters are fitted for each energy bin. The fitting results of the 25 energy bins of  $A_e$  and  $\tau$  are shown in Figure 4. Both  $A_e$  and  $\tau$  clearly show decreases with energy. An exponential decay function,  $p_0 \exp(-E/p_1)$ , is adopted to fit the energy dependences of  $A_e$  and  $\tau$ , resulting in  $\chi^2/\text{ndf} = 21.45/25$  and  $\chi^2/\text{ndf} = 34.42/25$ , respectively.

The amplitude can be well described by the exponential function. The fact that the FD amplitudes become smaller for higher energies can be easily understood as high-energy particles being less affected by the perturbed interstellar environment by the CME. Consequently, the energy spectra should also vary with time when an FD occurs (Belov et al. 2021), as they are expected to be harder during the FD. A single power-law fit to the energy spectrum between 4 and 20 GeV shows that the spectral index is  $\sim 2.85$  before the FD and  $\sim 2.70$  when the fluxes reach the minimum, and it becomes 2.85 after the FD. The energy dependence of the recovery time is, however, more complicated than the amplitude. It is interesting to compare the results obtained in this study with those by PAMELA. In Munini et al. (2018), the PAMELA experiment gave the energy dependences of the recovery time for electrons, protons, and helium nuclei, for rigidities from 0.6 GV to 10 GV. The qualitative behaviors of recovery time for these three types of particles are similar; all show an increase from 0.6 GV to 5 GV, although the specific values for electrons are different from that for nuclei. At higher energies, the recovery time for protons and helium nuclei decreases again. Due to the limited statistics, the decreasing behavior of the electron recovery time has not been observed. The DAMPE result clearly shows the decreasing behavior for the CRE recovery time above 2 GeV, which may indicate that the peaks of the recovery time for all particles are a few GeV. We can further see from Figure 4 that at high energies, the recovery time tends to be constant rather than continuing to decrease. The recovery time for protons by PAMELA may also show

<sup>25</sup> <http://www01.nmdb.eu/nest/>

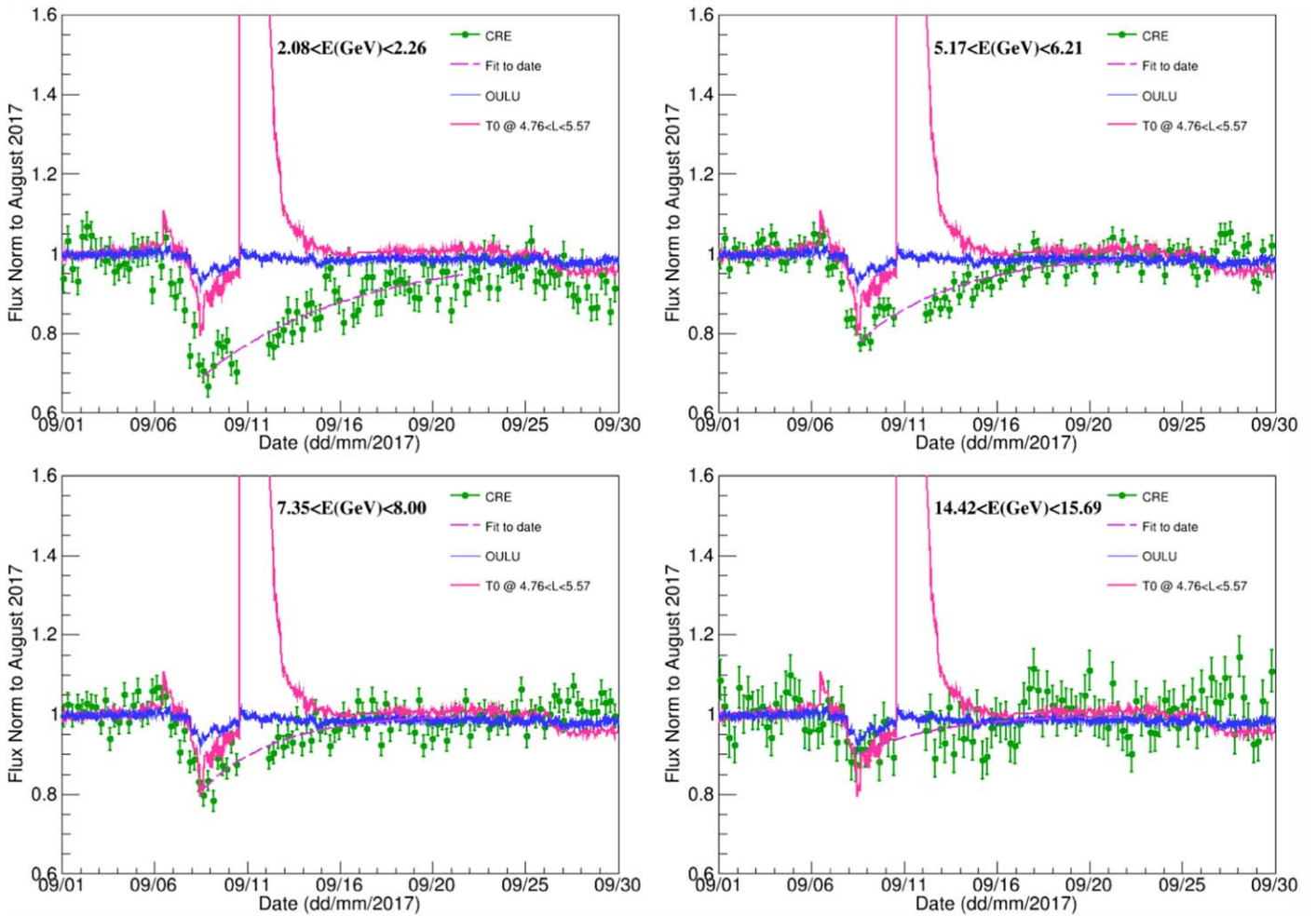


**Figure 3.** Time profiles of CRE fluxes in four energy bins from 00:00 UT of September 1 to 00:00 UT of 2017 October 1. The error bars are summations of statistical and systematic errors. In each plot, the T0 counting rates for  $4.76 < L < 5.57$  are shown in red and the OULU NM intensities are in blue.

such a flattening at high energies (Munini et al. 2018). But the errors, both for PAMELA protons and DAMPE CREs, are too large to clearly address this phenomenon.

The ground NMs can also measure the energy dependences of the FDs, although the energy resolution is relatively poor and the energy threshold is relatively high. As illustrated in Zhao & Zhang (2016), there are two types of energy dependences of the recovery time, one depends strongly on energies and the other remains almost independent of energies. It has been conjectured that the orientations and topologies of the CMEs may result in such differences (Zhao & Zhang 2016). However, a reliable energy determination of the NMs is difficult. For a specific NM station, a typical median energy  $E_M$  is defined as the value below which cosmic rays contribute to one-half of the counting rate. The median energy can be estimated as a function of cutoff rigidity  $R_c$  as  $E_M = 0.0877 R_c^2 + 0.154 R_c + 10.12$ , where  $E_M$  and  $R_c$  are in units of GeV and GV (Jämsén et al. 2007). The median energy is  $\sim 10$  GeV at the polar region and  $\sim 20$  GeV at the equator. The full behaviors of the recovery time in a wide energy range, especially for lower energies, are thus difficult for NMs to reveal. The energy dependence or independence of the recovery time shown by NMs may be only a part of the full energy dependence. For the event we discuss here, the CME travels toward the Earth. It should correspond to Event 2 of Zhao & Zhang (2016), and the recovery time is expected to be

a constant. Our results do not support such an expectation in general. However, the constant behavior may just be the reflection of the flattening above  $\sim 10$  GeV as shown in Figure 4. A more complete modeling of the recovery time versus the energies is necessary.

## 5. Modeling of the CRE FDs

Parker’s equation has been widely employed to describe the transport of charged particles in the heliosphere (Parker 1965). When the heliosphere has been disturbed by CMEs and the associated shocks, FDs of GCR fluxes can occur. This process can be modeled using the diffusion barrier model, which employs a moving diffusion barrier with different diffusion and drift parameters from those in the interplanetary space (Luo et al. 2018). Parker’s transport equation together with the diffusion barrier can be solved with the stochastic differential equation method (Zhang 1999; Strauss et al. 2011). We describe the method of modeling FDs in detail in Appendix B.

Given the proper model parameters, the FD behaviors of the DAMPE data can be reproduced, as shown in Figure 5 for select energy bands. We further derive the recovery time at different energies using Equation (2) and give the results in Figure 6. We can see that the model prediction is in good agreement with the data in the energy range of 2–20 GeV. However, this model may not precisely explain the detailed

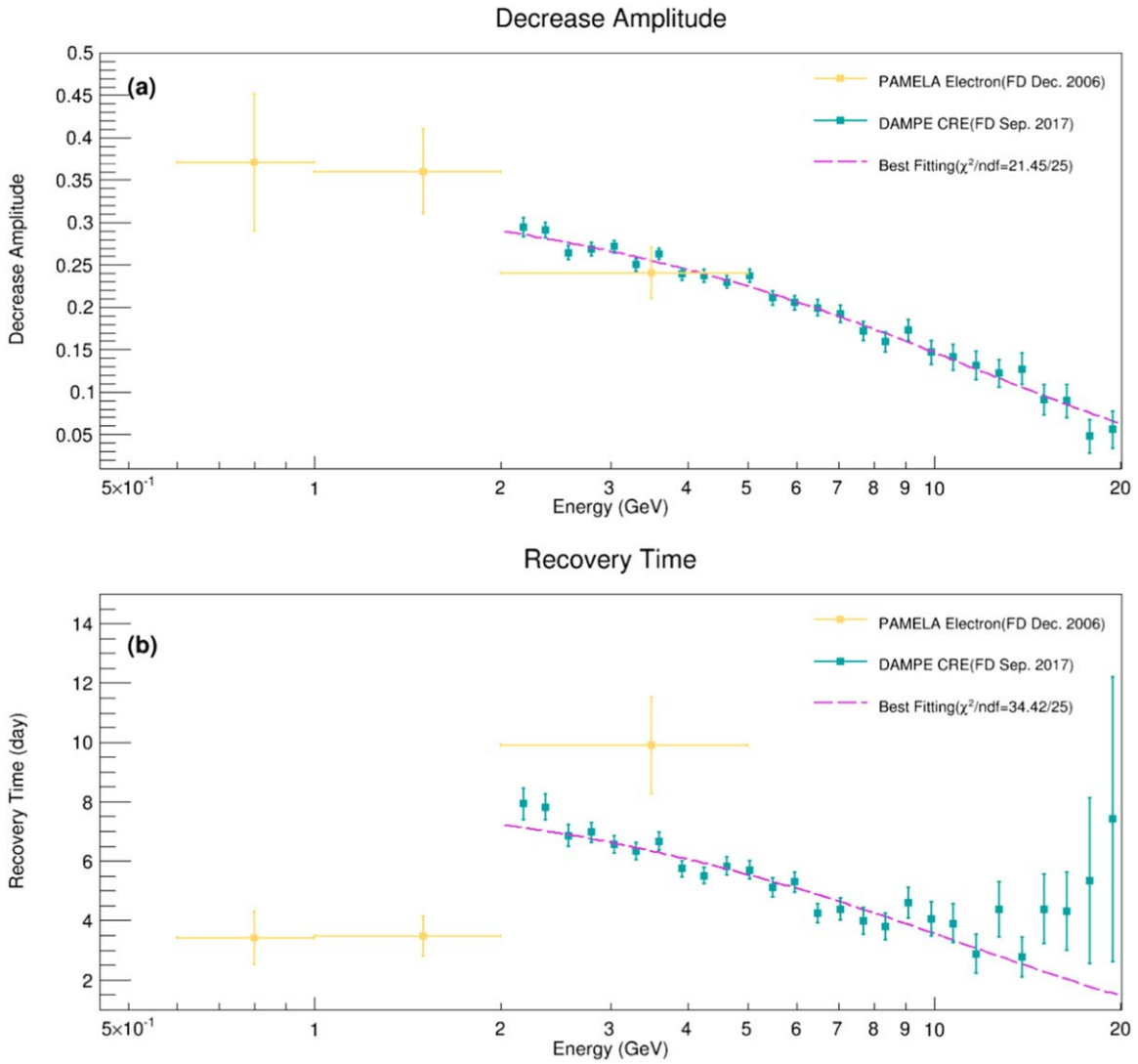


**Figure 4.** The decrease amplitude (panel (a)) and recovery time (panel (a)) vs. energy. Red solid lines show the best fits with an exponential function  $p_0 \exp(-E/p_1)$ .

behaviors of the data at higher or lower energies. The possible flattening at high energies, though more precise measurements are required to reach a conclusion, is not obvious in the modeling. Also the model predicts a longer recovery time at lower energies, which may not explain the turnover at a few GeV as indicated by the PAMELA and DAMPE data. Further refinement or modification of the FD modeling is thus necessary to fully account for the data.

## 6. Conclusion

In this work we give a detailed study of the CRE FDs associated with the CME that occurred in 2017 September and was observed by the DAMPE detector. A weak SEP event has been revealed through the T0 counting rate, while no unambiguous signal is shown by ground-based NMs. Meanwhile the high-precision time evolutions of CRE fluxes with a 6 hr time resolution have been obtained simultaneously. We study the energy dependences of the FD amplitudes and the recovery time and find that both decrease with energy. Together with the results of different particle species measured by PAMELA, this may show that the recovery time of all particle species increases below a few GeV and decreases at

higher energies. For energies above  $\sim 10$  GeV, the recovery time may become constant, which nevertheless requires more statistics to draw a firm conclusion. These results would give very important implications for modeling the propagation of GCRs in the heliosphere when there are disturbances from CMEs.

This study also illustrates the importance of direct measurements of FDs of various GCR species. Compared with the usually employed NM data, the direct measurements have the advantages of excellent particle identification, very good energy resolution, and much wider energy range coverage. More comparative studies of various FD events for different particle species observed by DAMPE in the future are expected to shed further light on the physics of particle transportation in the interplanetary environment.

The DAMPE mission is funded by the strategic priority science and technology projects in space science of the Chinese Academy of Sciences. In China the data analysis is supported by the National Key Research and Development Program of China (No. 2016YFA0400200), the National Natural Science Foundation of China (Nos. 11773085, U1738207, 11722328, 41774185, U1738205, U1738128, 11851305, 11873021, and

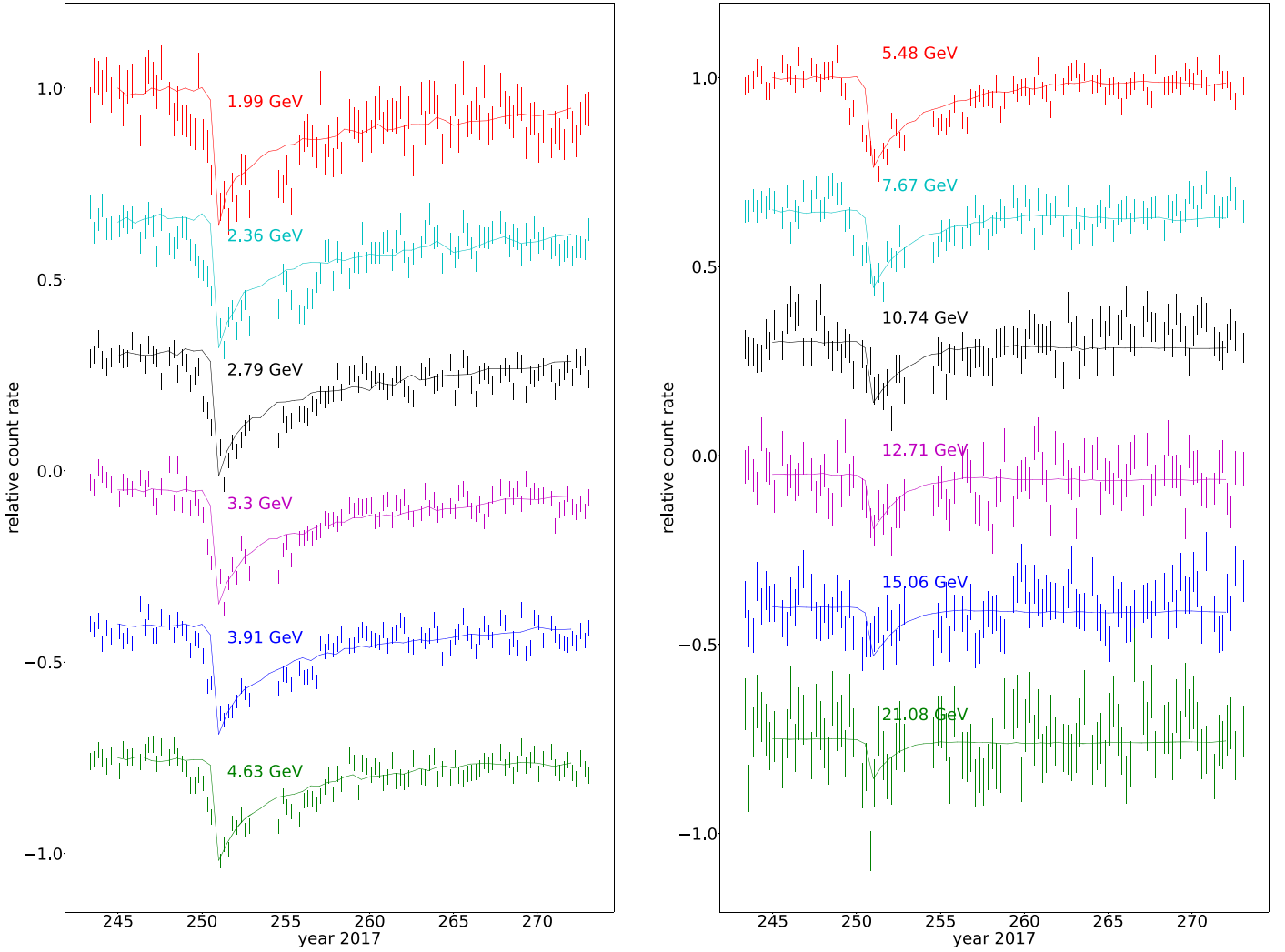


**Figure 5.** Variations of the relative CRE fluxes from the DAMPE observations (bars) and the FD model (lines). For visualization the results for different energies are gradually shifted downward with respect to the top one in each panel.

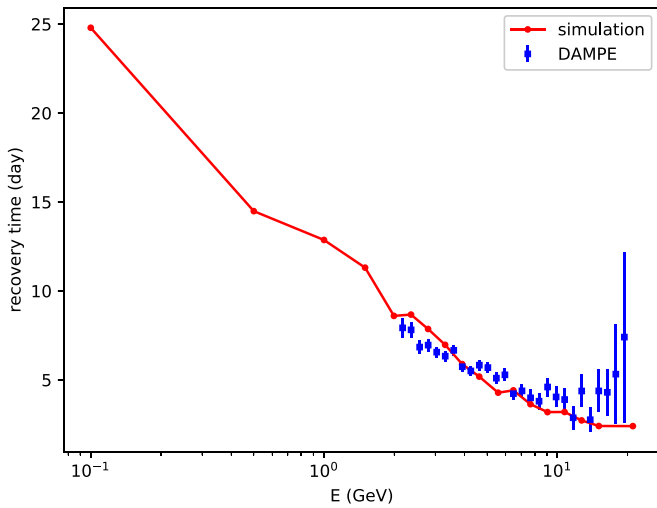


**Figure 6.** The recovery time of the model prediction compared with the DAMPE data.

U1631242), the strategic priority science and technology projects of the Chinese Academy of Sciences (No. XDA15051100), the 100 Talents Program of the Chinese

Academy of Sciences, the Young Elite Scientists Sponsorship Program by CAST (No. YESS20160196), and the Program for Innovative Talents and Entrepreneur in Jiangsu. In Europe the activities and the data analysis are supported by the Swiss National Science Foundation (SNSF), Switzerland and the National Institute for Nuclear Physics (INFN), Italy.

### Appendix A Parker's Transport Equation

Parker's transport equation is written as (Parker 1965)

$$\frac{\partial f}{\partial t} = -(\mathbf{V}_{\text{sw}} + \langle \mathbf{v}_d \rangle) \cdot \nabla f + \nabla \cdot (\mathbf{K}^{(s)} \cdot \nabla f) \quad (\text{A1})$$

$$+ \frac{1}{3}(\nabla \cdot \mathbf{V}_{\text{sw}}) \frac{\partial f}{\partial \ln p}, \quad (\text{A2})$$

where  $f(\mathbf{r}, p, t)$  is the particle distribution function,  $p$  is the momentum,  $\mathbf{V}_{\text{sw}}$  is the latitude-dependent solar wind speed (Potgieter et al. 2015; Luo et al. 2019), and  $\langle \mathbf{v}_d \rangle$  is the pitch-angle averaged drift velocity (Forman et al. 1974; Jokipii et al. 1977; Burger & Potgieter 1989; Engelbrecht & Burger 2015)



with the following form:

$$\langle v_d \rangle = \frac{pv}{3q} \nabla \times \frac{\vec{B}}{B^2}, \quad (\text{A3})$$

where  $q$  and  $v$  are the charge and velocity of the GCR particle, and  $\mathbf{B}$  is the magnetic field inside the heliosphere. The last term of Equation (A1) is the adiabatic energy loss.  $K^{(s)}$  is the symmetric diffusion tensor, given in the IMF aligned coordinates by

$$K^{(s)} = \begin{pmatrix} \kappa_{\parallel} & 0 & 0 \\ 0 & \kappa_{\perp\theta} & 0 \\ 0 & 0 & \kappa_{\perp r} \end{pmatrix}, \quad (\text{A4})$$

where  $\kappa_{\parallel}$  is the parallel diffusion coefficient, and  $\kappa_{\perp r}$  and  $\kappa_{\perp\theta}$  are two perpendicular diffusion coefficients in the radial and latitudinal directions. In our simulation, the diffusion coefficients are expressed as (Luo et al. 2019)

$$\kappa_{\parallel} = \kappa_{\parallel 0} \beta \frac{B_0}{B} \left( \frac{P}{P_k} \right)^a \left[ 1 + \left( \frac{P}{P_k} \right)^{\frac{b-a}{c}} \right]^c, \quad (\text{A5})$$

$$\kappa_{\perp r, \perp\theta} = (\kappa_{\perp r 0, \perp\theta 0}) \beta \frac{B_0}{B} \left( \frac{P}{P_k} \right)^a \left[ 1 + \left( \frac{P}{P_k} \right)^{\frac{b-a}{c}} \right]^c. \quad (\text{A6})$$

Here,  $\beta$  is the particle velocity in units of light speed;  $B$  is the magnitude of the local IMF with  $B_0 = 1$  nT;  $P$  is the rigidity;  $\kappa_{\parallel 0}$ ,  $\kappa_{\perp r 0}$ , and  $\kappa_{\perp\theta 0}$  are constants; and  $P_k$ ,  $a$ ,  $b$ , and  $c$  are free parameters that define the rigidity dependence of these diffusion coefficients.

We use the standard Parker field to describe the IMF (Parker 1958):

$$\mathbf{B}(r, \theta) = \frac{AB_{\oplus}}{r^2} \left( \mathbf{e}_r - \frac{r\Omega \sin \theta}{V_{\text{sw}}} \mathbf{e}_{\theta} \right) \times [1 - 2H(\theta - \theta_{\text{cs}})], \quad (\text{A7})$$

where  $B_{\oplus}$  is the reference value at the Earth position, which we take as the mean value of the last 13 months before the solar flare event,  $A = \pm 1 / \sqrt{\left(1 + \frac{\Omega^2}{V_{\text{sw}}^2}\right)}$  with the sign determining the polarity of the IMF.  $\Omega$  is the angular velocity of the Sun,  $H(\theta - \theta_{\text{cs}})$  is the Heaviside function, and  $\theta_{\text{cs}}$  determines the polar extent of the heliospheric current sheet (HCS). We model the HCS with the following analytical expression (Kota & Jokipii 1983),

$$\cot \theta_{\text{cs}} = -\tan \alpha \sin \phi^*. \quad (\text{A8})$$

Here,  $\alpha$  is the HCS tilt angle, which we also adopt as the mean value of the last 13 months,  $\phi^* = \phi + \frac{r\Omega}{V_{\text{sw}}}$ , with  $\phi$  being the longitude angle of the current sheet surface. We do not consider the phase of the corotating HCS.

The magnitude of drift in the HCS can be specified as (Burger & Potgieter 1989)

$$v_{\text{HCS}} = \frac{v}{6} \times \frac{4R_g}{r} \delta(\theta - \theta_{\text{cs}}), \quad (\text{A9})$$

where  $R_g$  is the gyroradius of the GCR particle and  $v$  is the particle's speed. Following Luo et al. (2013) and Luo et al.

(2017), we replace  $\delta(\theta - \theta_{\text{cs}})$  with  $r/(4R_g)$  within the distance of  $(-2R_g, 2R_g)$  to the HCS. By defining  $\psi$  as the angle between the local current sheet normal direction  $\mathbf{n}$  and the  $-\mathbf{e}_{\theta}$  direction, the drift vector of the current sheet can be written as

$$\mathbf{V}_{\text{cs}} = \frac{v}{6} (\mathbf{e}_r \sin \Phi \cos \psi + \mathbf{e}_{\theta} \sin \psi + \mathbf{e}_{\phi} \cos \Phi \cos \psi), \quad (\text{A10})$$

with  $\Phi$  being the IMF winding (spiral) angle.

## Appendix B The Diffusion Barrier Model

In our model, we use a 3D geometry profile to describe the propagating diffusion barrier. The diffusion and drift coefficients inside the barrier are expressed as

$$\kappa'_{\parallel, \perp, T} = \frac{\kappa_{\parallel, \perp, T}}{1 + \rho h(\theta) f(r) g(\phi)}. \quad (\text{B1})$$

In the above equation,  $\kappa'_{\parallel, \perp}$  ( $\kappa'_T$ ) are the diffusion (drift) coefficients inside the barrier,  $\rho$  is a constant determining the reduction level of the diffusion and drift coefficients, and  $h(\theta)$ ,  $g(\phi)$ , and  $f(r)$  describe the geometry of the diffusion barrier

$$h(\theta) = e^{-\left(\frac{\theta - \theta_0}{\theta_{\text{br}}}\right)^{10}}, \quad (\text{B2})$$

$$g(\phi) = e^{-\left(\frac{\phi}{\phi_{\text{br}}}\right)^{10}}, \quad (\text{B3})$$

$$f(r) = \begin{cases} 1 - \frac{r - r_{\text{cen}}}{r_a}, & r_{\text{cen}} < r < r_{\text{sh}} \\ \frac{r - r_{\text{end}}}{r_b}, & r_{\text{end}} < r \leq r_{\text{cen}} \\ 0, & \text{otherwise} \end{cases} \quad (\text{B4})$$

Here,  $\theta_0 = \pi/2$  means that the diffusion barrier hits the Earth head on; the parameters  $\theta_{\text{br}}$  and  $\phi_{\text{br}}$  denote the extensions of the diffusion barrier along the  $\mathbf{e}_{\theta}$  and  $\mathbf{e}_{\phi}$  directions;  $r_{\text{sh}}$ ,  $r_{\text{cen}}$ , and  $r_{\text{end}}$  are the radial distances of the front, center, and end locations of the barrier; and  $r_a = r_{\text{sh}} - r_{\text{cen}}$  and  $r_b = r_{\text{cen}} - r_{\text{end}}$  are widths of the leading and trailing paths of the barrier. In our model, we assume  $r_a = 0.5$  au,  $r_b = 0.3$  au,  $\theta_{\text{br}} = 60^\circ$ , and  $\phi_{\text{br}} = 180^\circ$ . The velocity of the diffusion barrier is adopted to be  $1500 \text{ km s}^{-1}$ , as given in the CME list<sup>26</sup>.

## Appendix C The Stochastic Differential Equation Method

Based on Ito's formula, Parker's equation can be solved numerically with the stochastic differential equation (SDE) technique (Zhang 1999; Strauss et al. 2011), with

$$d\mathbf{X} = (\nabla \cdot \mathbf{K}^{(s)} - \mathbf{V}_{\text{sw}} - \langle v_d \rangle) ds + \sum_{\sigma=1}^3 \tilde{\alpha}_{\sigma} dW_{\sigma}(s), \quad (\text{C1})$$

$$dp = \frac{p}{3} (\nabla \cdot \mathbf{V}_{\text{sw}} ds), \quad (\text{C2})$$

where  $dW_{\sigma}(s)$  is the Wiener process, which can be numerically generated by the Gaussian random number, and  $\sum_{\sigma} \alpha_{\sigma}^{\mu} \alpha_{\sigma}^{\nu} = 2\kappa^{\mu\nu}$ . The SDE method gives the time-dependent





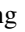

<sup>26</sup> [https://cdaw.gsfc.nasa.gov/CME\\_list/](https://cdaw.gsfc.nasa.gov/CME_list/)

solution of Equation (A1) as (Zhang 1999; Luo et al. 2019)

$$f(t, \vec{X}, p) = \langle f_b^i(t - \chi_i, \vec{X}_i, p_i) \rangle. \quad (C3)$$

$\langle f_b^i(t - \chi_i, \vec{X}_i, p_i) \rangle$  is the mean value for the pseudo-particles reaching the boundary  $(\vec{X}_i, p_i)$  at the first exit time  $\chi_i$ . In our calculation, the local interstellar spectrum of electrons are adopted from Zhu et al. (2021). The small fraction of positrons has been neglected.

### ORCID iDs

YiZhong Fan  <https://orcid.org/0000-0002-8966-6911>  
 Kun Fang  <https://orcid.org/0000-0002-1209-349X>  
 Piergiorgio Fusco  <https://orcid.org/0000-0002-9383-2425>  
 Fabio Gargano  <https://orcid.org/0000-0002-5055-6395>  
 Francesco Loparco  <https://orcid.org/0000-0002-1173-5673>  
 Mario Nicola Mazziotta  <https://orcid.org/0000-0001-9325-4672>  
 JingJing Zang  <https://orcid.org/0000-0002-2634-2960>  
 YaPeng Zhang  <https://orcid.org/0000-0003-1569-1214>  
 Li Feng  <https://orcid.org/0000-0003-4655-6939>  
 Xi Luo  <https://orcid.org/0000-0002-4508-6042>

### References

- Ambrosi, G., An, Q., Asfandiyarov, R., et al. 2019, *APh*, 106, 18  
 An, Q., Asfandiyarov, R., Azzarello, P., et al. 2019, *SciA*, 5, eaax3793  
 Azzarello, P., Ambrosi, G., Asfandiyarov, R., et al. 2016, *NIMPA*, 831, 378  
 Badruddin, B., Aslam, O. P. M., Derouich, M., Asiri, H., & Kudela, K. 2019, *SpWea*, 17, 487  
 Belov, A., Papaioannou, A., Abunina, M., et al. 2021, *ApJ*, 908, 5  
 Burger, R. A., & Potgieter, M. S. 1989, *ApJ*, 339, 501  
 Burlaga, L. 2015, *JPCS*, 642, 012003  
 Chang, J., Ambrosi, G., An, Q., et al. 2017, *APh*, 95, 6  
 Chertok, I. M., Belov, A. V., & Abunin, A. A. 2018, *SpWea*, 16, 1549  
 DAMPE Collaboration, Ambrosi, G., An, Q., et al. 2017, *Natur*, 552, 63  
 Dong, T., Zhang, Y., Ma, P., et al. 2019, *Aph*, 105, 31  
 Engelbrecht, N. E., & Burger, R. A. 2015, *AdSpR*, 55, 390  
 Forbush, S. E. 1937, *PhRv*, 51, 1108  
 Forman, M. A., Jokipii, J. R., & Owens, A. J. 1974, *ApJ*, 192, 535  
 Guo, J., Lillis, R., Wimmer-Schweingruber, R. F., et al. 2018, *A&A*, 611, A79  
 Hess, V. F., & Demmelmair, A. 1937, *Natur*, 140, 316  
 Huang, Y.-Y., Ma, T., Yue, C., et al. 2020, *RAA*, 20, 153  
 Hubert, G., Pazianotto, M. T., Federico, C. A., & Ricaud, P. 2019, *JGRA*, 124, 661  
 Jämsén, T., Usoskin, I. G., Rähkä, T., Sarkamo, J., & Kovaltsov, G. A. 2007, *AdSpR*, 40, 342  
 Jokipii, J. R., Levy, E. H., & Hubbard, W. B. 1977, *ApJ*, 213, 861  
 Kota, J., & Jokipii, J. R. 1983, *ApJ*, 265, 573  
 Livada, M., & Mavromichalaki, H. 2020, *SoPh*, 295, 115  
 Luo, X., Potgieter, M. S., Bindi, V., Zhang, M., & Feng, X. 2019, *ApJ*, 878, 6  
 Luo, X., Potgieter, M. S., Zhang, M., & Feng, X. 2017, *ApJ*, 839, 53  
 Luo, X., Potgieter, M. S., Zhang, M., & Feng, X. 2018, *ApJ*, 860, 160  
 Luo, X., Zhang, M., Feng, X., & Mendoza-Torres, J. E. 2013, *JGRA*, 118, 7517  
 Ma, P.-X., Zhang, Y.-J., Zhang, Y.-P., et al. 2019, *RAA*, 19, 082  
 Munini, R., Boezio, M., Bruno, A., et al. 2018, *ApJ*, 853, 76  
 Parker, E. 1965, *P&SS*, 13, 9  
 Parker, E. N. 1958, *ApJ*, 128, 664  
 Meyer, Peter, & Vogt, Rochus 1961, *JGR*, 66, 3950  
 Potgieter, M. S., Vos, E. E., Munini, R., Boezio, M., & Di Felice, V. 2015, *ApJ*, 810, 141  
 Smart, D. F., & Shea, M. A. 2005, *AdSpR*, 36, 2012  
 Strauss, R. D., Potgieter, M. S., Büsching, I., & Kopp, A. 2011, *ApJ*, 735, 83  
 Tykhonov, A., Ambrosi, G., Asfandiyarov, R., et al. 2018, *NIMPA*, 893, 43  
 Tykhonov, A., Ambrosi, G., Asfandiyarov, R., et al. 2019, *NIMPA*, 924, 309  
 Walt, M. 2005, in Introduction to Geomagnetically Trapped Radiation, ed. Martin Walt (Cambridge: Cambridge Univ. Press) 2005., -1  
 Xu, Z.-L., Kaikai, D., Shen, Z.-Q., et al. 2018, *RAA*, 18, 027  
 Yu, Y., Sun, Z., Su, H., et al. 2017, *Aph*, 94, 1  
 Zhang, M. 1999, *ApJ*, 513, 409  
 Zhang, Z., Zhang, Y., Dong, J., et al. 2015, *NIMPA*, 780, 21  
 Zhang, Z., Wang, C., Dong, J., et al. 2016, *NIMPA*, 836, 98  
 Zhao, L. L., & Zhang, H. 2016, *ApJ*, 827, 13  
 Zhu, C. R., Yuan, Q., & Wei, D. M. 2021, *Aph*, 124, 102495